X-RAY DIAGNOSTICS OF COSMIC PHOTOIONIZED PLASMAS

T. R. Kallman
Laboratory for High Energy Astrophysics
NASA/Goddard Space Flight Center

INTRODUCTION

Photoionized plasmas are important in a large fraction of cosmic X-ray sources. These include some of the brightest sources in the sky, and the most extensively studied, in addition to some of the faintest and most exotic. The diagnostic techniques used in studying these plasmas are still in an imperfect stage of development, and they differ significantly from many of those used to study the more familiar coronal plasmas. In this paper I will discuss the importance of photoionization as contrasted with coronal equilibrium, point out where these differences are likely to be most important, and summarize some of the experimental issues associated with X-ray astronomy and the modelling techniques used in interpreting observational data. The greatest part of the paper will be devoted to presentation of specific examples of the application of these techniques to photoionized plasmas.

The importance of photoionization can be evaluated by considering the ratio of the rates of collisional ionization to photoionization. These rates involve, respectively, averages over the electron velocity distribution and the photon energy distribution of the relevant cross sections. Crudely, the ratio of photoionization to collisional ionization rate can be approximated as: $(\int \sigma_{photoionization}(\varepsilon) F_\varepsilon d\varepsilon/\varepsilon)/(\int \sigma_{collisionalionization}(v) v f(f) dv) \simeq 2 \times 10^{10} f \xi T^{-3/2}$ where $\xi = 4\pi F/n$ is known as the 'ionization parameter', n is the gas density, T is the gas temperature, F_ε is the X-ray (energy) flux spectral distribution, F is the total X-ray (energy) flux, and f is a factor which reflects the extent to which the radiation spectrum overlaps the opacity distribution of the gas in question. Plausible values for ionization parameter range from $\leq 10^{-3}$ for the diffuse interstellar medium in our galaxy, for example, to $\sim 10^5$ for gas near a binary X-ray source. It is straightforward to show that objects with strong sources of radiation in the vicinity, such as binary X-ray stars, active galaxies and quasars, or H II regions are likely to be photoionization dominated, while objects such as the remnants of supernovae or the diffuse interstellar medium far from nearby stars are not as strongly affected by photoionization. The coronae of stars are exposed to intense radiation fields, but with a poor match between the energies of the ionizing photons and the opacity of the gas, so that photoionization is probably not dominant in these objects.

The objects in which photoionization is dominant include some of the most exotic in astronomy. X-ray binaries are likely to contain a collapsed degenerate star such as a neutron star, a white dwarf or possibly a black hole. Active galaxies may be associated with massive black holes, the remnant of the coalescence of a dense cluster of stars. Such objects are intrinsically difficult to study, owing to their relatively small size and the intense radiation and gravitational fields in their vicinity. Study of the reprocessed radiation can provide information which is not available from any other technique. Since the spectrum we observe depends on the conditions in the reprocessor, fitting of observed spectra can constrain the temperature, density, and element abundances. The dependence of the state of X-ray ionized gas on ionization parameter means that the density is determined as a ratio to the strength of the radiation field at the reprocessor. If the density can be constrained independently then we can infer the separation of the source and reprocessor. Also of interest are the elemental abundances, or their ratio to the 'cosmic' values (eg. Withbroe, 1971). Gas motions can be inferred from Doppler shifts or broadening of features such as lines or edges. These, in turn, can constrain the force due to gravity in the reprocessor. Lags between the variability in the continuum and the reprocessed spectrum provide a measure of the light travel time between the continuum source and reprocessor. In this paper I will illustrate with a few examples the use of spectral diagnostics of X-ray photoionized plasmas to answer some of these questions.

RECOMBINATION LINE EMISSION

X-ray Line emission from photoionized objects has been observed with several experiments, including the solid state and grating spectrometers on the *Einstein* (HEAO-2) satellite, and the Broad Band X-ray Telescope (BBXRT) flown as part of the ASTRO-1 mission in the space shuttle in late 1990. Such emission is most obvious in the 0.5-2 KeV energy range, and near 6-7 KeV. The low energy emission poses a challenge for interpretation owing partly to the limited resolving power of the experiments so far. This does not generally allow the separation of individual line components from their neighbors, necessitating spectrum synthesis and model fitting in order to learn about the conditions in the emitting gas. Such models involve considerable detail: treatment of a variety of atomic processes, including photoionization, various recombination processes, charge transfer, ionization and excitation by thermal electrons and by non-thermal photoelectrons; the attendant heating, cooling, emission and absorption associated with these processes; and consideration of these processes for all the ions of the elements which are most likely to be abundant in astrophysical systems.

Photoionized plasmas differ in several important ways from the coronal plasmas which are more familiar in many laboratory and astrophysical applications. First, owing to the influence of photoionization the temperature is lower at a given ionization level in the photoionized case than in the coronal case. Line emission is predominantly by radiative recombination cascades and dielectronic recombination rather than by electron collisional excitation. This leads to distinctly different emission spectra from individual ions. For example, for ions in the lithium through neon isoelectronic sequences recombination cascades tend to populate the 3s levels and thus favor the 3s-2p lines, while electron collisions populate the 3d levels and lead to stronger lines from the decay of these levels (Liedahl, et al., 1990). Recombination also leads to free-bound continuum emission, and the continua may be sufficiently narrow to mimic line emission when viewed with the limited resolving power of most past instruments. Figure 1 shows the spectra emitted by neon-like iron under the assumption of coronal equilibrium (panel a) and photoionization equilibrium (panel b). In the former case the spectrum is dominated by the $\sim$15 $\AA$ 3d-2p lines, while the latter is dominated by the $\sim$17$\AA$ 3s-2p lines. Second, photoionization produces a broader range of ion species for a given set of conditions than does coronal equilibrium. This is due to the fact that the spectra of the photons responsible for ionization in most astrophysical sources are much broader than a maxwellian electron velocity distribution. This is illustrated in figures 2 and 3, which show the ion abundance distributions as a function of temperature for the two different cases. It should be emphasized that in the case of photoionization it is the ionization parameter, not temperature, which is most important in determining ionization balance. These effects combine to produce distinctively different spectra for the two ionization scenarios, even when 'normalized' to some standard quantity. This is demonstrated in Figure 4, which shows the results of a synthetic spectrum assuming photoionization (panel a) and coronal equilibrium (panel b), with parameters chosen so that both produce approximately equal ion fractions of O^{+7}.

Considerations such as these are particularly important when analyzing the low energy X-ray line spectra from astrophysical sources. The solid curves in Figure 5 shows a spectrum from a bright binary X-ray source, Cygnus X-2, as observed by the grating spectrometers on the *Einstein* (HEAO-2) satellite. The underlying continuum has been subtracted from the spectrum shown here. The spectrum is as notable for the lines which are absent as for those which are seen. The ions most likely to contribute to the spectrum at these energies are the most cosmically abundant: oxygen and iron. However, the strong 15$\AA$ line of Fe XVII, and the Lα line of O VIII near 19$\AA$ are weak or absent. Dominant lines are near 17 $\AA$ and near 14 $\AA$, and may be due to photoionized Fe XVII and to higher ionization stages of iron, respectively. From figures 2 and 3 it is apparent that there is significant overlap in parameter space between O VIII and Fe XVII, suggesting that the abundance of oxygen may be far less than its cosmic value. The dashed curve in figure 5 represents an attempt at modelling this spectrum using a photoionized plasma consisting of pure iron with a superposition of components of various ionization parameters and emission measures; clearly, although the positions of the strongest observed features can be reproduced by the model, the constrast between these features and the 'gaps' between them are not reproduced. In spite of this, it is most likely that the emitting gas is photoionized and that oxygen is underabundant relative to iron.

IRON K LINES

The K lines of iron have a unique importance in X-ray astronomy. Observationally, they fall in a region of the spectrum which is relatively free of confusion due to lines from other elements, photoelectric absorption, and features due to absorption in the instrument; iron is the most abundant heavy ($Z\geq 10$) element in the sun. In photoionized plasmas lines are formed as a direct result of K shell ionization, and the rate of line formation is only weakly dependent on the ionization state and temperature of the gas over a wide range of conditions.

The most easily observable quantities are the line strength and the line energy. Iron line strength can be parameterized in at least two ways: the photon flux in the line, or the equivalent width (ratio of line flux to flux in the adjacent continuum). In a photoionized gas the strength depends primarily on the number of photons absorbed by ionizing iron; the lines are an effective 'bolometer' for exciting photons near 10 KeV. The energies of the iron K lines are probes of the ionization state in the gas near the compact object. Lines near 6.4 KeV (1.94 $\mathring{A}$) are emitted by ions between neutral and neon-like (Fe XVII). The lines emitted by higher ion stages range in energy up to $\sim$7 KeV for Fe XXVI. Photoionized and coronal plasma models predict different equivalent widths for these lines, since in coronal models the adjacent continuum is likely to be dominated by thermal continuum emission (e.g. recombination and bremsstrahlung) from the same gas responsible for the iron line, while in photoionized models the adjacent continuum is likely to be affected by the incident continuum photons, i.e. those responsible for the inner shell ionization of iron. The relative amounts of iron line and continuum in the photoionized case depend on the geometry, as illustrated in figure 6: the observer may see more of the incident continuum than the line emitting gas if the reprocessor has holes in it, or the observer may see less if there is an opaque object along the line of sight.

Figure 7 shows locus of the iron line mean energy and equivalent width for various photoionized and coronal models, with the photoionized model equivalent widths calculated according to the assumptions of case (II) above. For photoionization models the equivalent widths shown in figure 7 must also be modified to take into account geometrical effects and the column density of the reprocessor; the values shown correspond to a reprocessor column density of 10^{24} cm^{-2}. At greater column densities the equivalent width is reduced by absorption of line photons within the reprocessor, and by the fact that the incident continuum photons penetrate the reprocessor with reduced efficiency. At lower column densities the equivalent width is approximately proportional to column, i.e. $EW = EW_0(N/10^{24}cm^{-2})(\Omega/(4\pi))$. Here Ω is the solid angle subtended by the reprocessor relative to the fraction of continuum photons which reach the observer. The panels in figure 6 thus correspond to $\Omega \leq 4\pi$, Ω=4π, and $\Omega \geq 4\pi$, respectively.

From figure 7 it is apparent that equivalent width for emission of low energy lines ($\varepsilon \leq$ 6.5 KeV) is very much less for the coronal plasma than for the photoionized plasma. This is due to the fact that the low energy lines arise from ion stages Fe XVIII and below, while collisional excitation from the K to L shells can only occur for ion stages Fe XVIII and above, with the phase space for the transition depending on how nearly full is the L shell. In photoionized plasmas the fluorescence yeild depends only weakly on the state of ionization of iron. Furthermore, the line equivalent width is larger than in the photoionized model for iron lines with energies greater than 6.5 KeV (1.9 $\mathring{A}$), although this result depends on the geometrical assumptions as described above. Thus one clear signature of photoionized plamsas in the iron lines is low energies ($\varepsilon \simeq$6.4 KeV), and if so then the equivalent width provides information about the geometry and column density of the reprocessing gas.

An illustration of the utility of iron lines in diagnosing photoionized gases is given by the observations of the Seyfert 2 galaxy NGC 1068. Objects of this class have active nuclei, as evidenced by strong emission lines in the optical and ultraviolet. In NGC 1068 the lines which are most suggestive of activity, the broad lines of permitted transitions of hydrogen, are highly polarized (Miller and Goodrich, 1990). The most likely explanation for this phenomenon is that the broad line emitting gas is seen only in reflection. The reflector is highly ionized gas which scatters photons into our line of sight by electron scattering. Iron line observations allow a test of this model, since the reflector is likely to emit iron line photons directly. Figure 8a shows the spectrum of NGC1068 taken with the Japanese X-ray astronomy satellite $Tenma$ (Koyama, et al., 1989), showing a strong broad iron line with energy 6.6 KeV and equivalent width 2 KeV. According to figure 7 such a line could be emitted by a coronal plasma at 10^7K. However, the continuum shape near the line is adequately represented by a pure power law, not thermal emission as predicted by coronal models. More likely is a photoionized plasma in which our direct line of sight to the continuum source is blocked, consistent with the hypothesis of a hidden active nucleus.

More recently, NGC 1068 was observed at higher spectral resolution ($\varepsilon/\Delta\varepsilon \simeq 50$ in the iron line region) by the Broad Band X-ray Telescope (BBXRT) instrument. The spectrum, shown in figure 8(b), reveals that the iron K line can be modelled by 3 narrow components at 6.4, 6.65 and 6.97 KeV, with equivalent widths of 1.2, 0.78, and 0.74 KeV, respectively (Marshall et al., 1993). Clearly the 6.4 KeV line is indicative of photoionization, and implies a column density and solid angle for the reprocessor which satisfy $(N/10^{24}cm^{-2})(\Omega/(4\pi)) \simeq 1$. The other two line components cannot be emitted by a photoionized gas with the same temperature or ionization parameter as the gas emitting the 6.4 KeV line; this additional gas component must have an ionization parameter $\xi \geq 10^3$ erg cm s^{-1} if it is photoionized. Again, the shape of the continuum argues against coronal emission for these lines. Thus, the iron K lines provide us with evidence in favor of the existence of the hidden nucleus, and provide important clues as to the ionization state and therefore the density of the gas responsible for line emission.

WARM ABSORBER

All astrophysical X-ray spectra are affected by photoelectric absorption by material along the line of sight to the photon source. Such material may be quite far from the source and thus unaffected by the radiation from the source. Photoelectric absorption by neutral material is affected by both the shape of the photoionization cross section, and by the relative abundances of the various elements in the absorbing gas. For abundances close to those inferred for the sun (e.g. Withbroe, 1972) elements heavier than helium never contribute more than approximately 50% of the total opacity at any energy between 1 Ry and 1 KeV (e.g. Morrison and McCammon, 1978). If so, the opacity distribution in this range of photon energies can be characterized as an approximately ε^{-3} decrease punctuated by modest discontinuities at the K shell thresholds of the various abundant trace elements such as C, O, Ne, Si, and S. This universal shape has served as an adequate description of the data from many objects.

If, on the other hand, absorbing gas is close enough to the source to be appreciably heated and ionized, then the opacity can be considerably affected. Measurements of the opacity then can serve to constrain the ionization state of the absorbing gas and hence, via modelling, the conditions in the absorber. The opacity distributions from partially ionized absorbers resemble the neutral absorber at the highest energies where absorption is detected, typically near 1 KeV, but have reduced opacities at lower energies. This is interpreted as being due to ionization of the lighter elements responsible for opacities at low energies, H, He, and C, while heavier elements which dominate the opacities at high energies, O, Ne, and

Mg, are more nearly neutral. This is consistent with the predictions of ionization balance models in which lighter elements are more easily ionized under a given set of conditions than are heavier elements. Figure 9 shows examples of the opacity distribution of ionized absorbers for various conditions. Each panel plots the photoabsorption cross section per hydrogen nucleus scaled by ε^3 for various conditions. Panel (a) shows the behavior of a coronal plasma, and panels (b) and (c) show photoionized plasmas for differing choices of the ionizing continuum (Krolik and Kallman, 1984). The approximate ε^3 scaling of the opacity of neutral material is apparent from the top curve in each panel, which corresponds to low temperature or ionization parameter. Increasing temperature or ionization parameter results in a progressive decrease in opacity at the lowest photon energies, with a much smaller reduction at high energies. Thus, an ionized absorber can be characterized as being 'leaky' at low energies when compared to a neutral absorber. Comparison of panels (b) and (c) shows the effect of differing ionizing spectra on the distribution: panel (c), with a harder ionizing spectrum, shows more of a reduction in opacity at high energies (near the iron K edge) than does panel (b) for high ionization parameters. The difference between the opacity from a coronal gas and the photoionized gas shown in panel (b) is negligible given the accuracy of current models. However, photoionization is a more plausible mechanism for producing an ionized absorber since the ionization can be produced by the same continuum which is passing through the absorber.

An example of the use of photoelectric absorption in diagnosing photoionized plasmas comes from the BBXRT observations of the Seyfert 1 galaxy NGC 4151. This object is thought to contain an active nucleus which is not hidden from our direct line of sight (owing to the presence of strong unpolarized lines in the UV spectrum). Figure 10 shows the count spectrum (Weaver, et al., 1992) observed with BBXRT together with fits to a neutral absorber (panel a) and to a photoionized absorber (panel b). It is clear that there is an excess of counts below 1 KeV above the best fit model shown in panel a, while the ionized absorber adequately fits the data at these energies. The ionization parameter derived from the fit to panel (b) is log(ξ)=1.7, and the column density required is $N = 2.5 \times 10^{21} cm^{-2}$. Together with a luminosity estimate based on extrapolating that observed in the X-ray band, $L \simeq 10^{43}$ erg s^{-1}, these require that the absorber have a density $n \simeq 31.$ cm^{-3} and a distance from the continuum source of $\simeq 8 \times 10^{19}$ cm. This is approximately consistent with the expected position of the gas responsible for the emission of UV lines. However, the gas which absorbs the X-rays has very much greater ionization parameter; its existence could not have been inferred in the absence of X-ray spectral observations.

SUMMARY

X-ray astronomy dates from the beginning of the space program. In a short time experimental techniques have progressed by an amount comparable to what required 150 years in optical astronomy. The next few years are likely to see this trend continue, and diagnostic techniques are needed to make the best use of the new data. In order to do this work is needed to bring astrophysical modelling techniqes closer to those used in modelling laboratory plasmas, particularly in the area of the atomic physics assumptions and the various rate and cross section data incorporated in the codes. The development of new comprehensive computational programs and databases for dissemination of these quantities is particularly welcome in this regard.

REFERENCES

K. *o*, **y**, a.ma, K., et al., 1989; P. A. S. J.; 41; 731

K. *r*, **o**, l.ik, J.H. and Kallman, T.R., 1984; Astrophys. J.; 286; 366

L. *i*, **e**, d.ahl, D., Kahn, S.M., Goldstein, W., and Osterheld, A., 1990; Ap. J.; 350; L37

M. *a*, **k**, i.shima, K., 1986, in ; The Physics of Accretion onto Compact Objects;; K. O. Mason, M. G. Watson and N. E. White, eds, (Berlin: Springer-Verlag)

M. *a*, **r**, s.hall, F., et al., 1993; Ap. J.; 405; 168

M. *i*, **l**, l.er, J., and Goodrich, M., 1990; Ap. J.; 355; 456

M. *o*, **r**, r.ison, J., and McCammon, D., 1983; Ap. J.; 270; 119

O. *s*, **t**, e.rbrock, D. E., 1974; Astrophysics of Gaseous Nebulae ;; (San Francisco: W.H. Freeman and Co.)

R. *a*, **y**, m.ond J.C., and Smith, B. H., 1977; Ap. J. Supp.; 35; 419

W. *e*, **a**, v.er, K., et al., 1992; Ap. J.; 401; L11

W. *h*, **i**, t.e, N.E., Peacock, A., and Taylor, B.G. 1985; Ap. J.; 296; 475

W. *i*, **t**, h.broe, G., 1971, in; The Menzel Symposium on Solar Physics, Spectra, and Gaseous Nebulae;; ed. K. B. Gebbie (NBS SP353)

Figure 1: Spectra emitted by neon-like iron emitted under the assumption of coronal equilibrium at a temperature of 5×10^6K (panel a) and under the assumption of photoionization equilibrium at an ionization parameter of logξ=2 and a temperature of 10^5 K (panel b).
Figure 2: Fractional abundances of the ions of carbon, oxygen, neon, silicon, sulfur and iron vs. temperature (in units of 10^4 K) under the assumption of coronal equilibrium. For each element, ions are ordered in descending ionization state from right to left: fully stripped corresponds to the 'rightmost' curve, with progressively lower ionization states dominating at lower temperature.
Figure 3: Fractional abundances of the ions of carbon, oxygen, neon, silicon, sulfur and iron vs. temperature (in units of 10^4 K) under the assumption of photoionization equilibrium. The ionizing spectrum is assumed to be a 10 KeV bremsstrahlung spectrum. It should be pointed out that, in this case, the ionization parameter is the more relevant independent variable; temperature is used for illustration. For each element, ions are ordered in descending ionization state from right to left: fully stripped corresponds to the 'rightmost' curve, with progressively lower ionization states dominating at lower temperature.
Figure 4: Emitted line spectra from coronal (upper panel) and photoionized (lower panel) for conditions with approximately equal O VIII Lα line intensity.
Figure 5: Fits to the observed line spectrum from the X-ray binary Cygnus X-2 observed by the grating spectrograph on the *Einstein* (HEAO-2) satellite (solid curve). The dashed curve represents an attempt at modelling this spectrum using a superposition of model spectra similar to those shown in figure 4 at various ionization parameters.
Figure 6: Three different geometrical distributions for iron K line reprocessors: Observer sees more, the same, or less continuum than reprocessor (from Makishima, 1986).
Figure 7: Loci of the iron line mean energy and equivalent width for plasma models for coronal (solid) and photoionized plasmas (dashed line). The free parameters are temperature (coronal case) and ionization parameter, ξ (photoionized case, see text for definition), with values increasing monotonically as curves are traversed from right to left. The equivalent width units are eV. In the photoionized case the ionizing spectrum is taken to be a bremsstrahlung spectrum with a temperature of 10 KeV and a total luminosity of 10^{38} erg s^{-1}.
Figure 8: Observed spectra from the Seyfert 2 galaxy NGC 1068 taken from the *Ginga* satellite (upper panel; Koyama et al., 1988) and from the BBXRT experiment (lower panel; Marshall et al., 1992).
Figure 9: Examples of the opacity distribution of ionized absorbers for various conditions. Each panel plots the photoabsorption cross section per hydrogen nucleus scaled by ε^3 for various conditions. Panel (a) shows the behavior of a coronal plasma, and panels (b) and (c) show photoionized plasmas for differing choices of the ionizing continuum (Krolik and

Kallman, 1984).

Figure 10: Fitting the observed spectra from the Seyfert 1 galaxy NGC 4151 to a neutral absorber (lower panel) and an ionized absorber (upper panel). The points are the count rate spectrum as observed by BBXRT (Weaver, et al., 1992), and the solid curve is the best model fit.

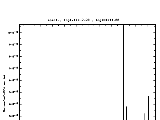
spect.. log(xi)=-2.28 , log(N)=11.00

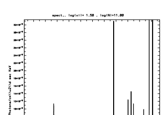
spect.. log(xi)= 1.50 . log(N)=11.00
Photons/cm\\u2\\d sec KeV

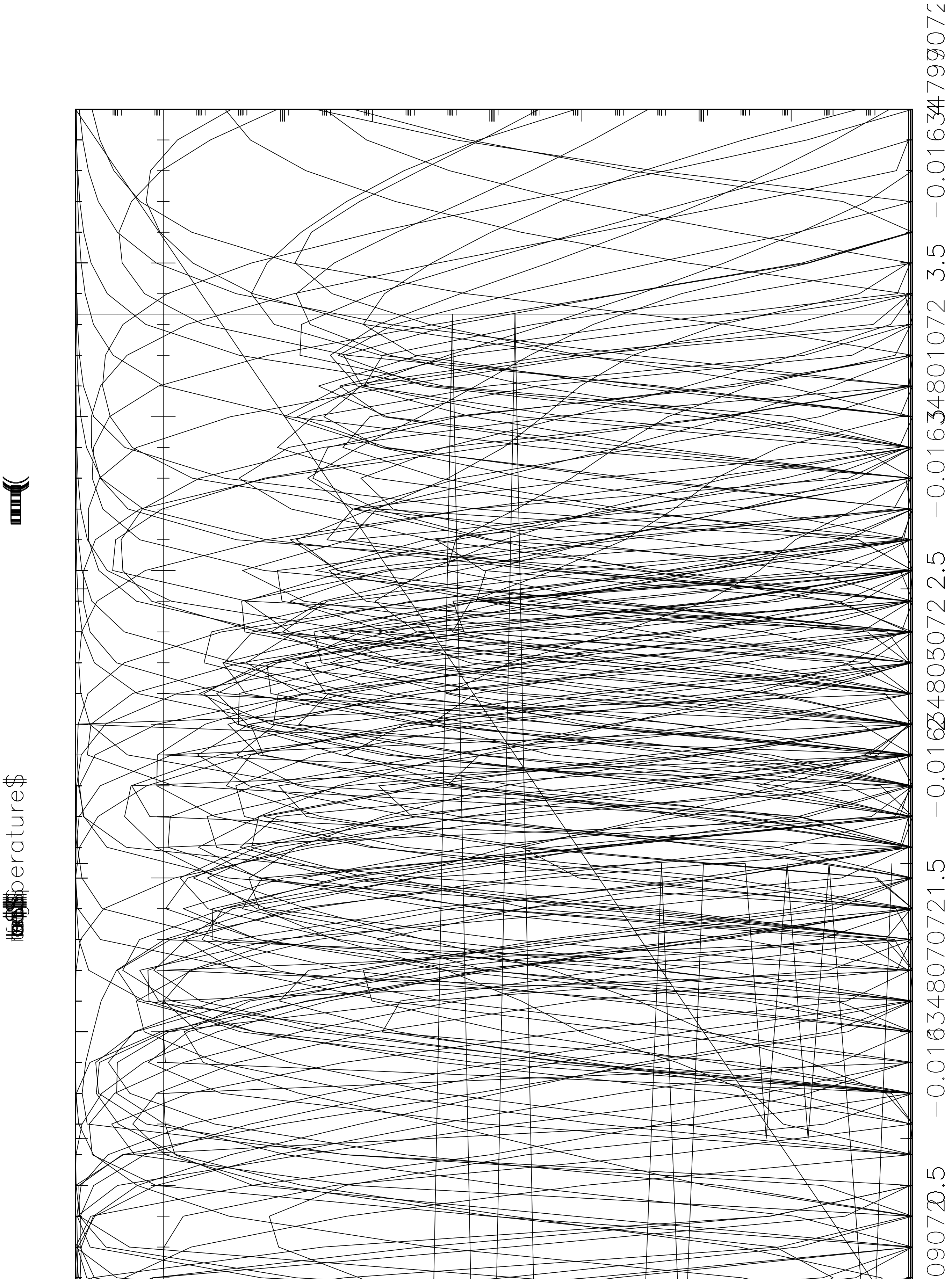

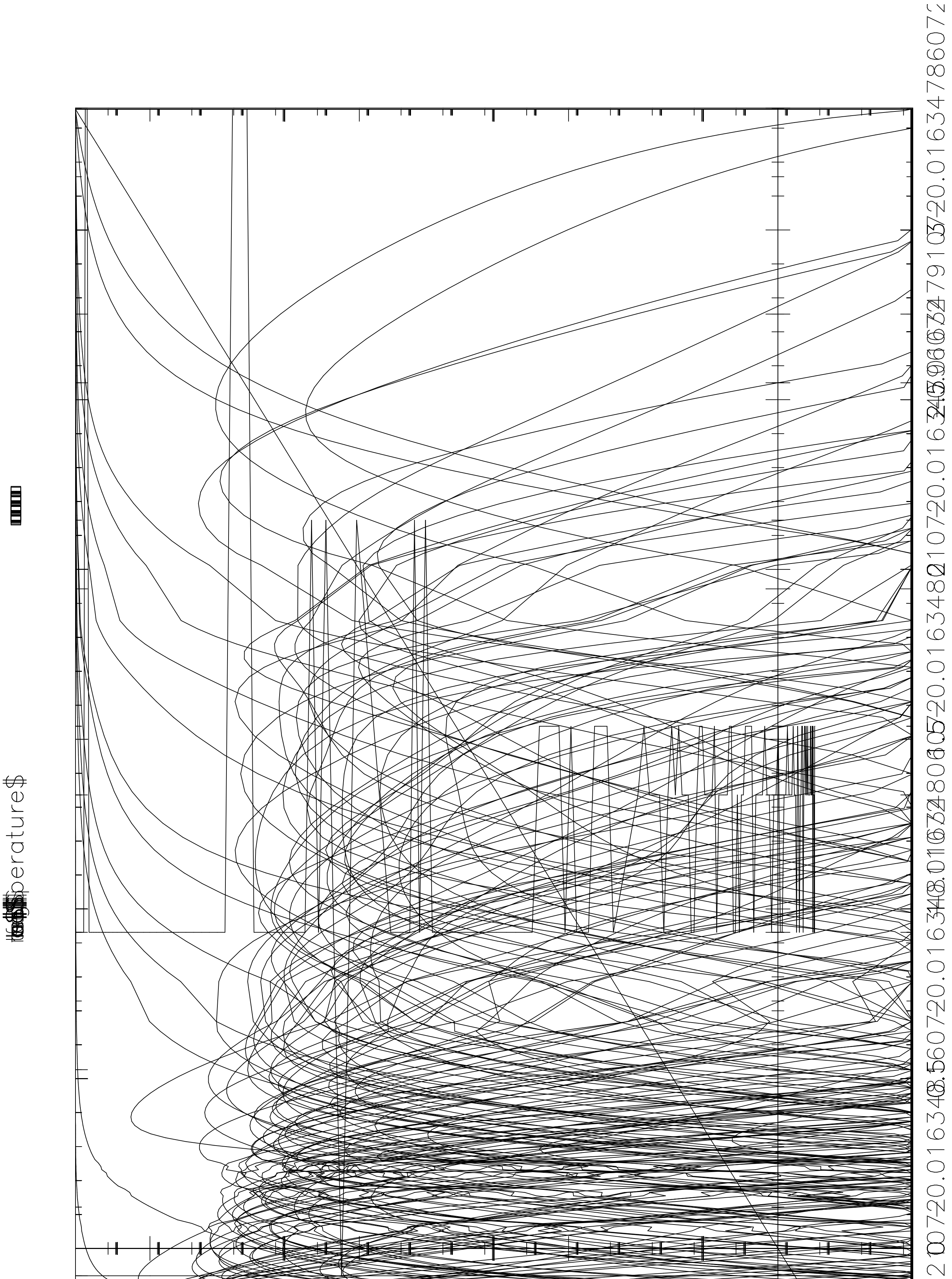

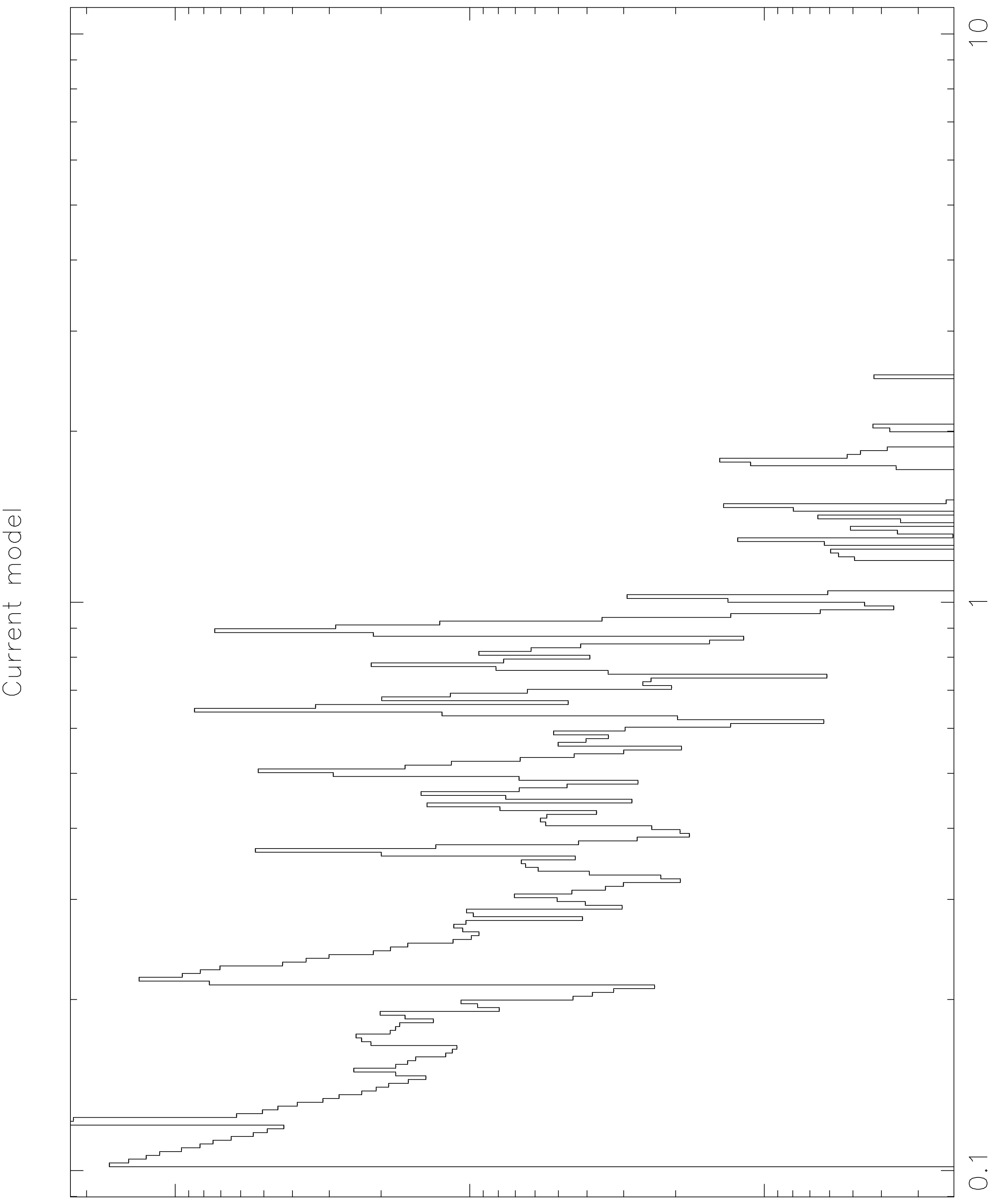
Current model
0.1
1
10

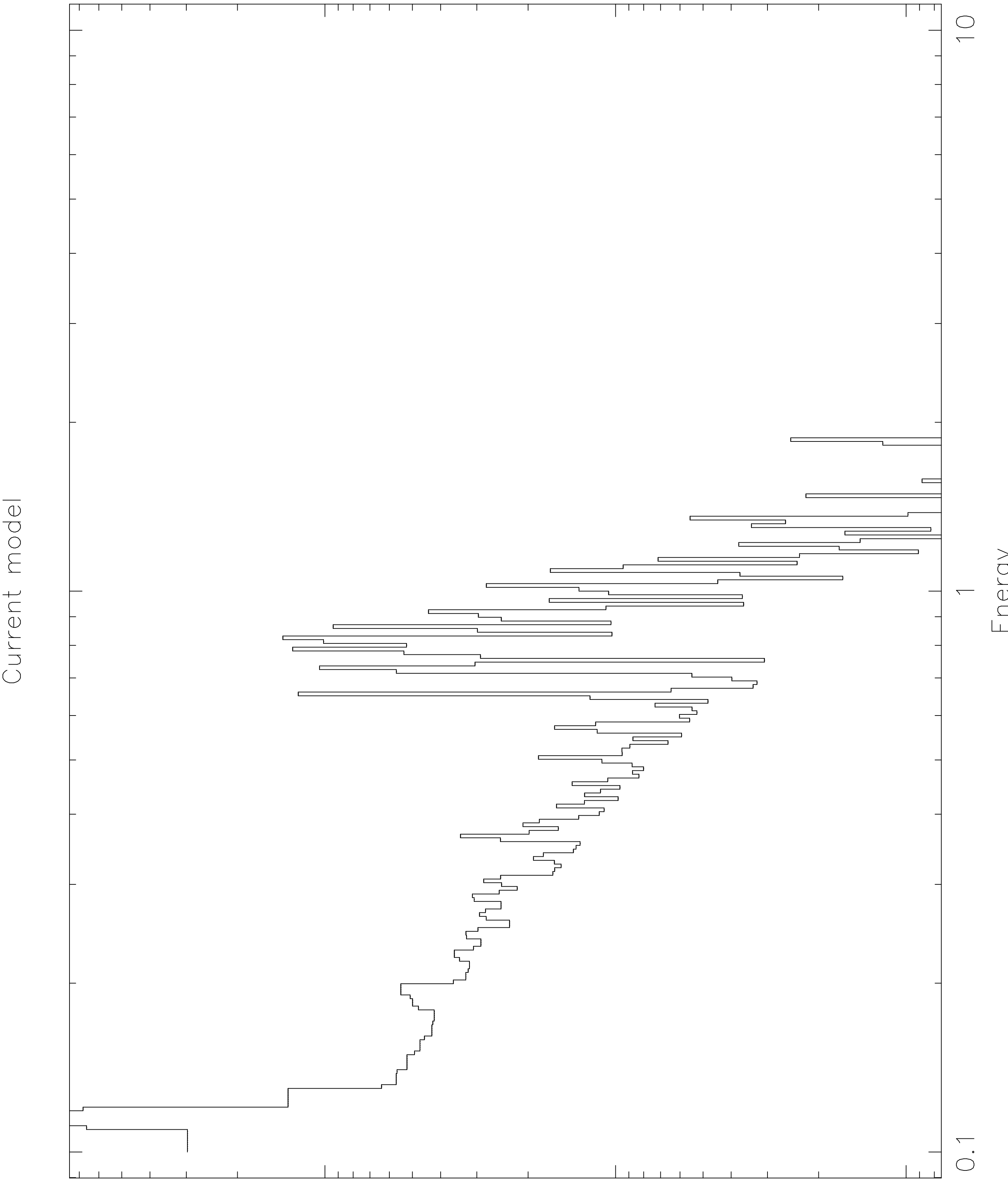

Current model
10
1
0.1

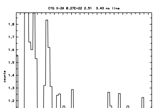
CYG X-2A 0.27E+22 2.51 3.43 no line
1.8
1.7
1.6
1.5
1.4
1.3
1.2
counts

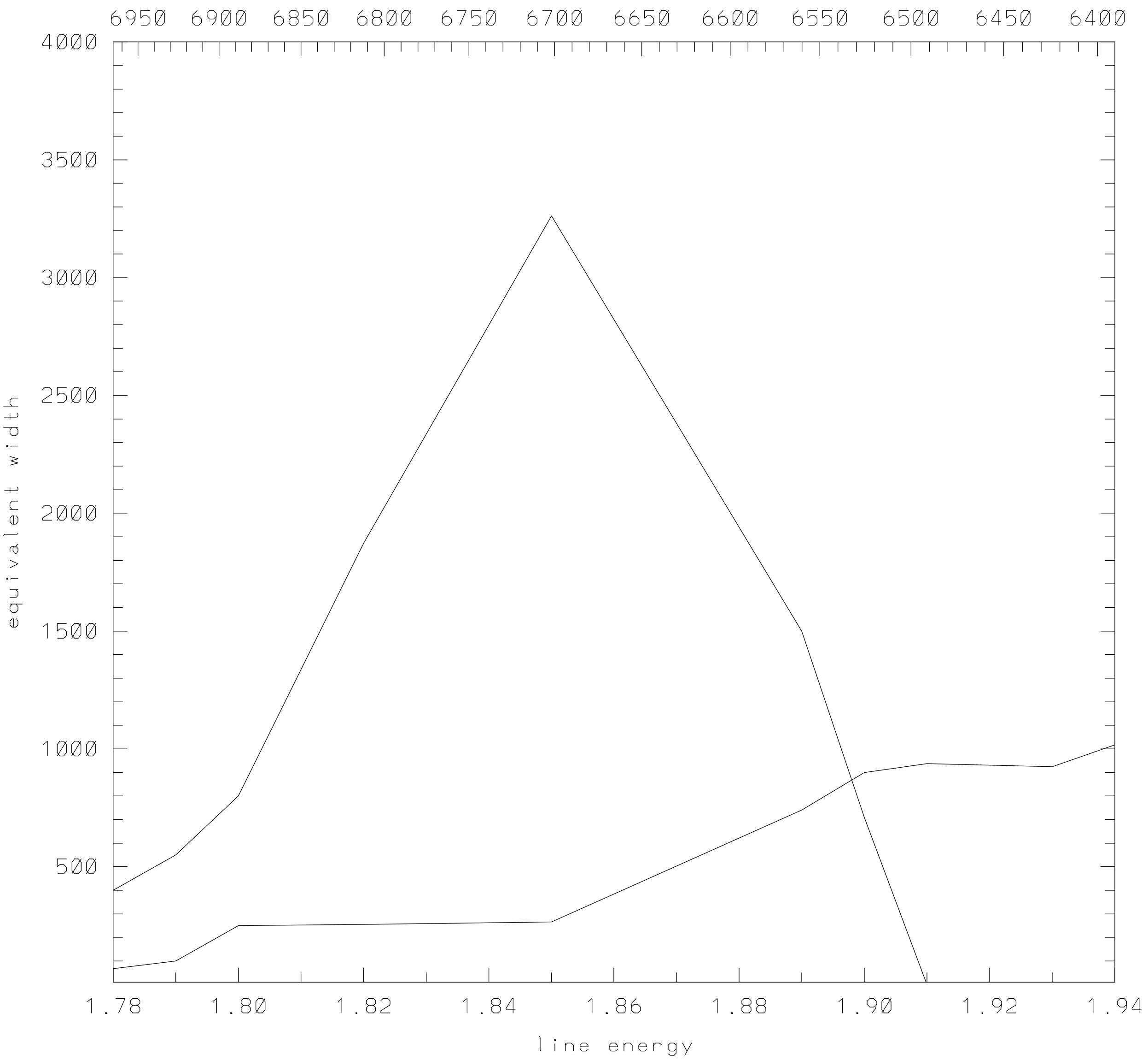
6950 6900 6850 6800 6750 6700 6650 6600 6550 6500 6450 6400
4000
3500
3000
2500
2000
1500
1000
500
equivalent width
1.78 1.80 1.82 1.84 1.86 1.88 1.90 1.92 1.94
line energy

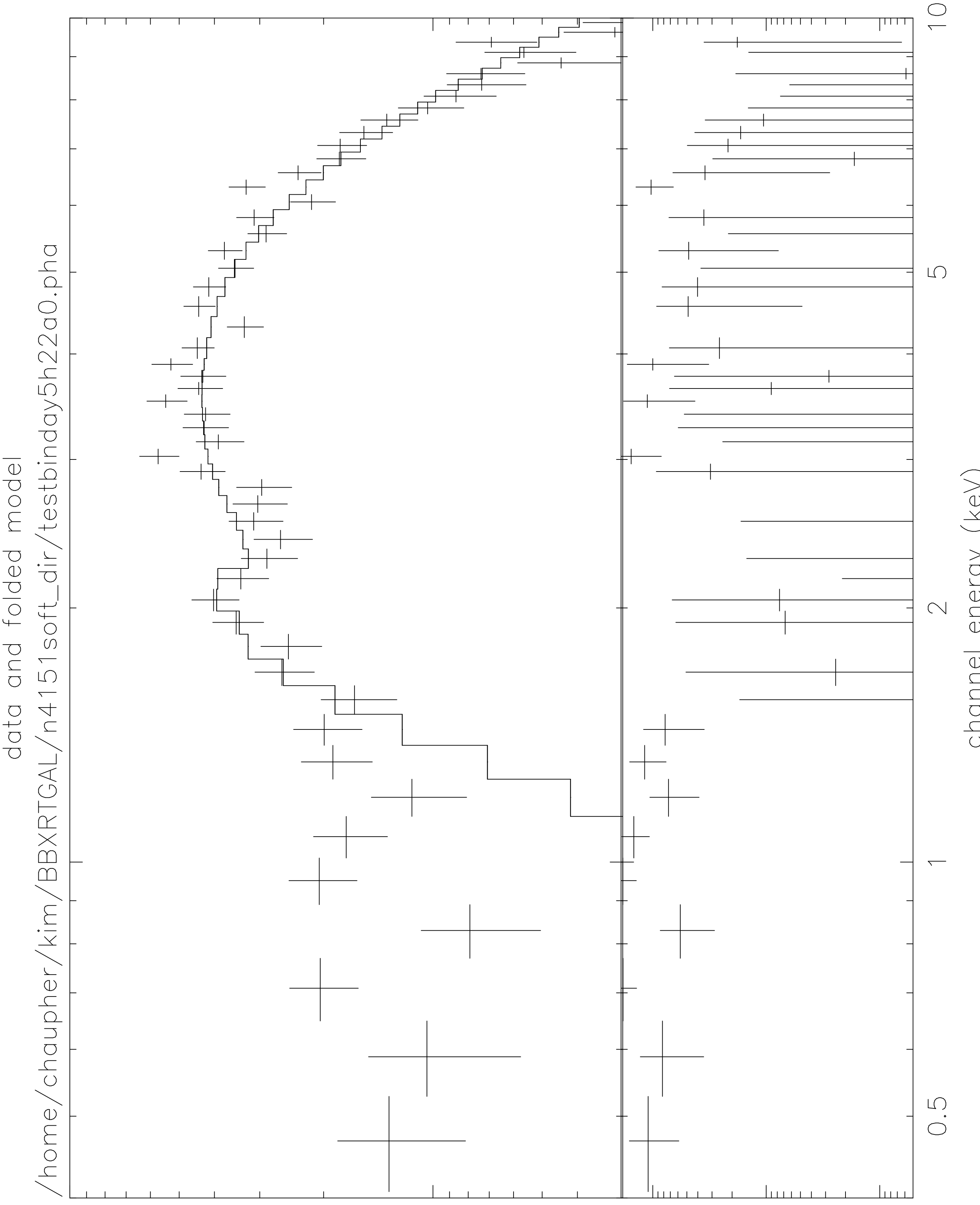
data and folded model
/home/chaupher/kim/BBXRTGAL/n4151soft_dir/testbinday5h22a0.pha
0.5
1
2
5
10
channel energy (keV)

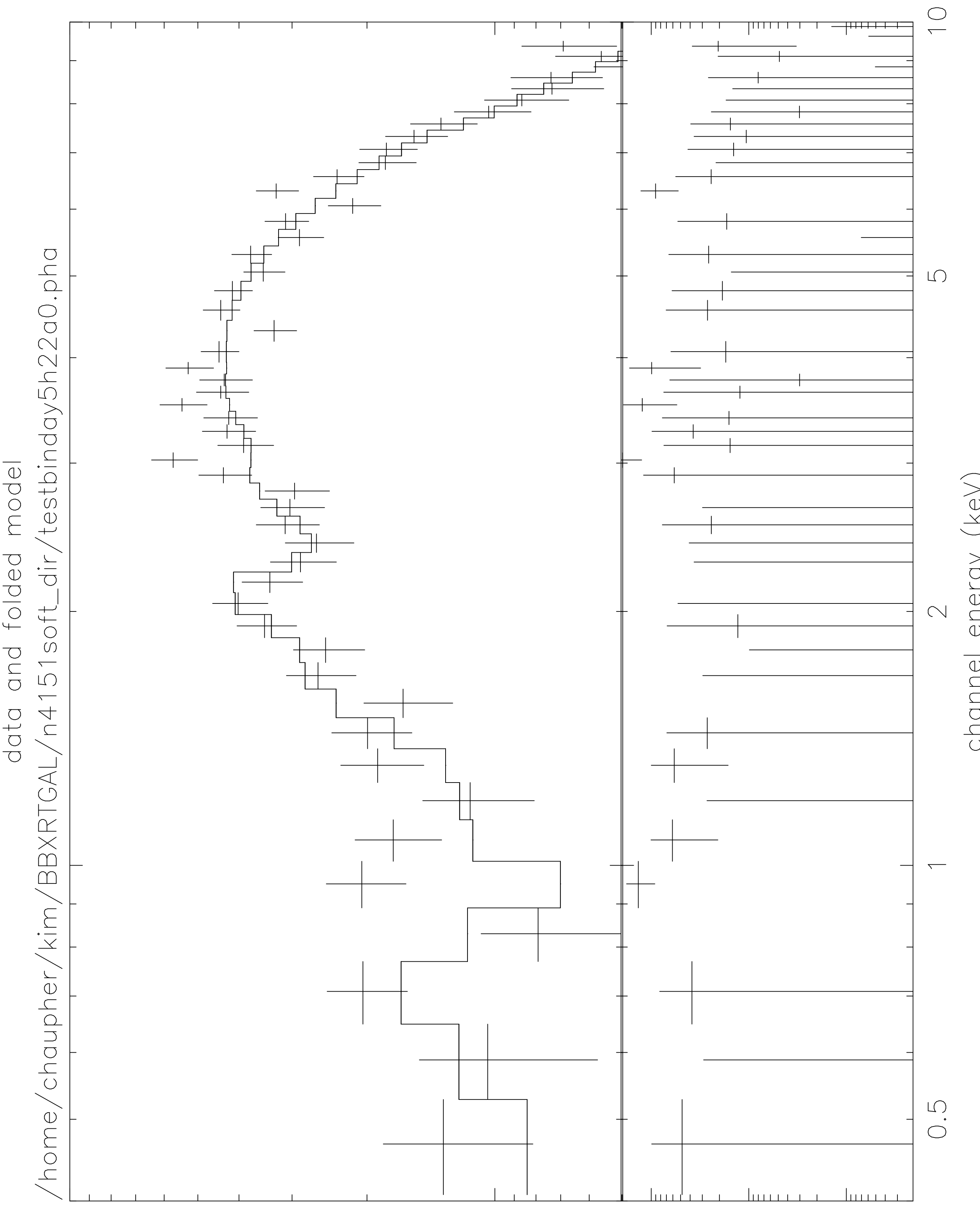
data and folded model
/home/chaupher/kim/BBXRTGAL/n4151soft_dir/testbinday5h22a0.pha
0.5
1
2
5
10